

AP-LDM: ATTENTIVE AND PROGRESSIVE LATENT DIFFUSION MODEL FOR TRAINING-FREE HIGH-RESOLUTION IMAGE GENERATION

Boyuan Cao, Jiaxin Ye, Yujie Wei, Hongming Shan[†]

Institute of Science and Technology for Brain-inspired Intelligence, Fudan University



Figure 1: **High-resolution images generated by our AP-LDM using a single 3090 GPU.** The corresponding thumbnails are generated by SDXL (Podell et al., 2023) at their training resolution.

ABSTRACT

Latent diffusion models (LDMs), such as Stable Diffusion, often experience significant structural distortions when directly generating high-resolution (HR) images that exceed their original training resolutions. A straightforward and cost-effective solution is to adapt pre-trained LDMs for HR image generation; however, existing methods often suffer from poor image quality and long inference time. In this paper, we propose an Attentive and Progressive LDM (AP-LDM), a novel, training-free framework aimed at enhancing HR image quality while accelerating the generation process. AP-LDM decomposes the denoising process of LDMs into two stages: (i) attentive training-resolution denoising, and (ii) progressive high-resolution denoising. The first stage generates a latent representation of a higher-quality training-resolution image through the proposed attentive guidance, which utilizes a novel parameter-free self-attention mechanism to enhance the structural consistency. The second stage progressively performs upsampling in pixel space, alleviating the severe artifacts caused by latent space upsampling. Leveraging the effective initialization from the first stage enables denoising at higher resolutions with significantly fewer steps, enhancing overall efficiency. Extensive experimental results demonstrate that AP-LDM significantly outperforms state-of-the-art methods, delivering up to a $5\times$ speedup in HR image generation, thereby highlighting its substantial advantages for real-world applications. Code is available at <https://github.com/kmittle/AP-LDM>.

[†]: Corresponding author.



Figure 2: **Comparison of our AP-LDM with prior work in generating 2048×2048 image.** The prompt is *Neon lights illuminate the bustling cityscape at night, casting colorful reflections on the wet streets.* Zoom-in for a better view.

1 INTRODUCTION

Diffusion models (DMs) have demonstrated impressive performance in visual generation tasks, particularly in text-to-image generation (Ho et al., 2020; Nichol & Dhariwal, 2021; Podell et al., 2023; Esser et al., 2024; Mou et al., 2024; Zhang et al., 2023; Feng et al., 2023). One notable variant of DMs is the latent diffusion model (LDM), which performs diffusion modeling in latent space to reduce training and inference costs, enabling high-resolution (HR) generation up to 1024×1024 . While it is possible to modify the input size for higher-resolution generation, this often results in severe structural distortions, as illustrated in Fig. 2(a). Therefore, a recent research focus is on adapting trained LDMs for HR image generation without the need for additional training or fine-tuning (*i.e.* training-free manner), which can inherit the strong generation capacities of existing LDMs, especially open-sourced versions like Stable Diffusion.

Existing training-free approaches for HR image generation can be roughly categorized into three types: sliding window-based, parameter rectification-based, and progressive upsampling-based. Sliding window-based methods first divide the HR image into several overlapping patches and use sliding window strategies to perform denoising (Bar-Tal et al., 2023; Haji-Ali et al., 2023; Lee et al., 2023). However, these methods could result in repeated structures and contents due to the lack of communication between windows; see Fig. 2(b). Parameter rectification-based methods attempt to correct models’ parameters for better structural consistency through the entropy of attention maps, signal-to-noise ratio, and dilation rates of the convolution layers (Jin et al., 2024; Hwang et al., 2024; He et al., 2023). Though efficient, they often lead to the degradation of texture details; see Fig. 2(c). Unlike the two types mentioned above, progressive upscaling-based methods are to iteratively upsample the image resolution, which maintains better structural consistency and shows state-of-the-art (SOTA) performance (Du et al., 2024; Lin et al., 2024). Unfortunately, these methods require fully repeating the denoising process multiple times, leading to an unaffordable computational burden; *e.g.*, AccDiffusion takes 26 minutes to generate a 4096×4096 image. In addition, their upsampling operation in the latent space may introduce artifacts; see Fig. 2(d). To sum up, existing methods fail to ensure the fast, high-quality HR image generation.

In this paper, we propose the attentive and progressive LDM, termed AP-LDM, a novel, training-free framework aimed at enhancing HR image quality while speeding up the generation process. Specifically, AP-LDM decomposes the denoising process of LDMs into two stages: (i) attentive training-resolution (TR) denoising, and (ii) progressive HR denoising. The first stage aims to generate a latent representation of a high-quality image at the training resolution through the proposed attentive guidance, which is implemented via a novel parameter-free self-attention mechanism to improve structural consistency. The second stage aims to progressively upsample the resolution in the pixel space rather than latent space, which can alleviate the severe artifacts caused by the latent space upsampling. By leveraging the effective initialization from the first stage, AP-LDM can perform denoising in the second stage with significantly fewer steps, enhancing the overall efficiency with $5\times$ speedup. Extensive experimental results demonstrate the effectiveness and efficiency of AP-LDM in generating HR images over the state-of-the-art baselines.

Contributions. The contributions of this work are summarized as follows. (i) We propose AP-LDM, a novel, training-free framework aimed at enhancing the HR high-quality generation while accelerating the generation process. (ii) We propose attentive guidance, which can utilize a novel parameter-free self-attention to improve the structural consistency of the latent representation to-

wards high-quality images at the training resolution. (iii) We propose progressively upsampling the resolution of latent representation in the pixel space, which can alleviate the artifacts caused by the latent space upsampling. (iv) Extensive experimental results demonstrate that the proposed AP-LDM significantly outperforms the SOTA models in terms of image quality and inference time, emphasizing its great potential for real-world applications.

2 RELATED WORK

HR image generation with super-resolution. An intuitive approach to generating HR images is to first use a pre-trained LDM to generate TR images and then apply a super-resolution model to perform upsampling (Wang et al., 2023; Zhang et al., 2021; Liang et al., 2021; Luo et al., 2024; Wang & Zhang, 2024). Although one can obtain structurally consistent HR images in this way, super-resolution models are primarily focused on enlarging the image, and shown to be unable to produce the details that users expect in HR images (Du et al., 2024; Lin et al., 2024).

HR image generation with additional training. Existing additional training methods either fine-tune existing LDMs with higher-resolution images (Hoogeboom et al., 2023; Zheng et al., 2024; Guo et al., 2024) or train cascaded diffusion models to gradually synthesize higher-resolution images (Teng et al., 2023; Ho et al., 2022). Though effective, these methods require expensive training resources that are unaffordable for regular users.

HR image generation in training-free manner. Current training-free methods can be roughly classified into three categories: sliding window-based, parameter rectification-based, and progressive upsampling-based methods. Sliding window-based methods consider spatially splitting HR image generation (Bar-Tal et al., 2023; Haji-Ali et al., 2023; Lee et al., 2023). Specifically, they partition an HR image into several patches with overlap, and then denoise each patch. However, due to the lack of communication between windows, these methods result in structural disarray and content duplication. While enlarging the overlaps of the windows mitigates this issue, it can result in unbearable computational costs. For the parameter rectification-based methods, some researchers discovered that the collapse of HR image generation is due to the mismatches between higher resolutions and the model’s parameters (Jin et al., 2024; Hwang et al., 2024; He et al., 2023). These methods attempt to eliminate the mismatches by rectifying the parameters such as the dilation rates of some convolutional layers. While mitigating the structural inconsistency, they often lead to the degradation of image details. Different from the aforementioned two types, the progressive upsampling-based methods show SOTA performance in some recent studies (Du et al., 2024; Lin et al., 2024). Though promising, they require fully repeating the denoising process multiple times, which incurs unbearable computational overhead. Additionally, these methods perform upsampling in the latent space, which may introduce artifacts.

These methods aforementioned fail to improve the quality of HR images and computational efficiency at the same time. In contrast to them, AP-LDM aims to enhance both HR images quality and the generation speed towards the real-world applications.

3 METHOD

3.1 OVERVIEW OF AP-LDM

Fig. 3 presents the overview of AP-LDM, which can adapt a pre-trained LDM to generate HR images without further training. Formally, a pre-trained LDM utilizes a denoising U-Net model \mathcal{F} to iteratively denoise the latent representation of size $h \times w \times c$, which is then converted back to the pixel space for final image generation through the decoder \mathcal{D} of a variational autoencoder (VAE). We note that the initial latent representation is sampled from a Gaussian distribution $\epsilon \sim \mathcal{N}(0, \mathbf{I})$, and for the inference the encoder \mathcal{E} of VAE is not involved.

Our AP-LDM extends the pre-trained LDMs for higher-resolution image generation in a training-free manner; *i.e.*, \mathcal{E} , \mathcal{D} and \mathcal{F} are fixed. AP-LDM achieves this by decomposing the standard denoising process in the latent space into two stages: (i) attentive training-resolution (TR) denoising, and (ii) progressive high-resolution (HR) denoising. In the first stage, AP-LDM aims to generate a latent representation of a higher-quality TR image through the proposed attentive guidance. The atten-

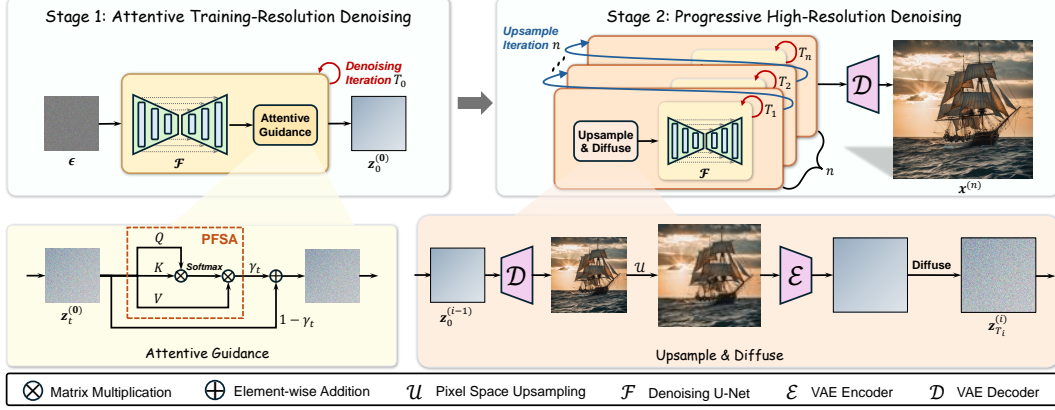


Figure 3: **Overview of AP-LDM.** AP-LDM divides the denoising process of a pre-trained LDM into two stages. The first stage leverages the introduced attentive guidance to enhance the structural consistency by utilizing a novel parameter-free self-attention mechanism (PFSA). The second stage iteratively upsamples the latent representation in pixel space to eliminate artifacts.

tive guidance is implemented as linearly combining the novel parameter-free self-attention (PFSA) and the original latent representation to improve the structural consistency. In the second stage, AP-LDM uses the latent representation provided by the first stage as a better initialization, and iteratively obtains higher-resolution images via the pixel space upsampling and diffusion-denoising refinement.

We detail the attentive TR denoising in §3.2, followed by the progressive HR denoising in §3.3.

3.2 ATTENTIVE TRAINING-RESOLUTION DENOISING

Motivation. Enhancing the structural consistency helps improve image quality (Si et al., 2024). However, it is challenging to do this in a training-free manner. We observe that the self-attention mechanism presents powerful global spatial modeling capability (Vaswani et al., 2017; Han et al., 2021; Dosovitskiy et al., 2020; Liu et al., 2021), and this capability is parameter-agnostic. It is determined by the paradigm of global similarity calculation inherent to the self-attention mechanism (Vaswani et al., 2017; Zhou et al., 2024). These insights motivate us to consider designing a novel parameter-free self-attention mechanism to elegantly enhance the global structural consistency of the latent representation.

Denoising with attentive guidance. To improve the structural consistency of the latent representation at the training resolution $z \in \mathbb{R}^{h \times w \times c}$, we propose a simple yet effective parameter-free self-attention mechanism for attentive guidance, termed PFSA, formulated as:

$$\text{PFSA}(z) = \text{Flatten}^{-1} \left(\text{Softmax} \left(\frac{\text{Flatten}(z) \cdot \text{Flatten}(z)^T}{\lambda} \right) \cdot \text{Flatten}(z) \right), \quad (1)$$

where the operation Flatten reshapes the latent representation into shape $(hw) \times c$ and Flatten^{-1} reshapes it back; λ is the scaling factor, with a default value of $\lambda = \sqrt{c}$.

However, we empirically observe that directly using the PFSA in Eq. (1) to improve the structural consistency of the latent representation could lead to unstable denoising. Therefore, we propose linearly combining the outputs of PFSA and the original latent representation as attentive guidance, which is formulated as:

$$\tilde{z} = \gamma \text{PFSA}(z) + (1 - \gamma)z, \quad (2)$$

where \tilde{z} is the structurally enhanced latent representation and γ is the guidance scale.

As shown in Fig. 3, we append the attentive guidance in Eq. (2) to denoising U-net model \mathcal{F} and repeat the denoising process for a total of T_0 times for the first stage. We note that the denoising process starts from step T_0 to 0, and the final output of the first stage is denoted as $z_0^{(0)}$.

Adaptive guidance scale. Considering that the latent representation is mostly non-semantic noise in the first few steps of denoising, we delay k steps in introducing attentive guidance. Moreover,

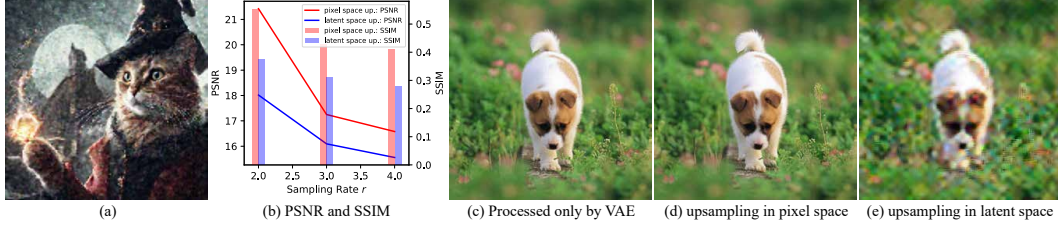


Figure 4: (a) AP-LDM generation with latent space upsampling leads to severe artifacts. (b) Quantitative analysis of PSNR and SSIM. (c) to (e): Qualitative comparisons of VAE-only process and upsampling in different spaces.

during the denoising process, the image structure is generated first, followed by local details (Yu et al., 2023; Teng et al., 2023). Therefore, we primarily employ attentive guidance in the early to mid-steps of denoising to focus on enhancing the structural consistency of the latent representation. Specifically, we introduce the adaptive guidance scale γ_t by applying a decay to a given guidance scale γ , formulated as:

$$\gamma_t = \begin{cases} \gamma \left[\frac{\cos\left(\frac{T_0 - k - t}{T_0 - k} \pi\right) + 1}{2} \right]^\beta & \text{if } t \leq T_0 - k, \\ 0 & \text{otherwise,} \end{cases} \quad (3)$$

where β is the decay factor. In practice, considering that k depends on T_0 for different resolutions, we use a delay rate $\eta_1 = \frac{k}{T_0}$ to control the number of steps for delaying attentive guidance.

3.3 PROGRESSIVE HIGH-RESOLUTION DENOISING

Motivation. Fig. 2(a) shows that pre-trained LDMs still retain some ability to generate high-frequency information when directly used to synthesize HR images, although they exhibit structural disarray. Therefore, intuitively, we can utilize the latent representation produced by the first stage as a structural initialization, and generate the HR images through the “upsample-diffuse-denoise” iteration in the latent space. However, this pipeline leads to severe artifacts, as shown in Fig. 4(a). We speculate that this is due to *the upsampling of latent representations in the latent space*.

Pilot study. To examine this hypothesis, we conduct the following experiments. Specifically, we randomly select 10k images from ImageNet (Deng et al., 2009) to create an image set \mathcal{P} . For each image $x \in \mathcal{P}$, we perform the following operations to obtain three additional image sets: (i) $\hat{x} = \mathcal{D} \circ \mathcal{E}(x)$, which use VAE to obtain the reconstructed image set \mathcal{P}_{ref} ; (ii) $\hat{x} = \text{up} \circ \mathcal{D} \circ \mathcal{E} \circ \text{down}(x)$, which performs upsampling in pixel space to obtain the image set \mathcal{P}_{pix} ; and (iii) $\hat{x} = \mathcal{D} \circ \text{up} \circ \mathcal{E} \circ \text{down}(x)$, which performs upsampling in latent space to obtain the image set \mathcal{P}_{lat} . Both upsampling up and downsampling down are performed using bicubic interpolation. Fig. 4(b) reports the quantitative results, where r represents the upsampling or downsampling rate. We calculate the PSNR and SSIM for pixel space upsampling set \mathcal{P}_{pix} and latent space upsampling set \mathcal{P}_{lat} with respect to the reference set \mathcal{P}_{ref} . It can be clearly observed that the latent space upsampling leads to a significant performance decline compared to pixel space upsampling. Fig. 4(c) to (e) shows upsampling in the pixel space produces images close to the reference while upsampling in latent space leads to severe artifacts and detail loss.

Progressive HR denoising with pixel space upsampling. Based on the above conclusion, we propose performing upsampling in the pixel space rather than latent space and utilize diffusion and denoising to refine the upsampled higher-resolution image. Specifically, the second stage consists of n sub-stages to progressively upsample the training-resolution to target resolution, each corresponding to one upsampling operation. For i -th sub-stage, $i = 1, \dots, n$, we prepend an upsample and diffuse operation before the denoising process, which can be defined as:

$$z_{T_i}^{(i)} = \sqrt{\bar{\alpha}_{T_i}} \hat{z}_0^{(i-1)} + \sqrt{1 - \bar{\alpha}_{T_i}} \epsilon, \quad \text{where } \hat{z}_0^{(i-1)} = \mathcal{E}(\mathcal{U}(\mathcal{D}(z_0^{(i-1)}))), \quad (4)$$

where $\bar{\alpha}_{T_i}$ is the noise schedule hyper-parameter of the T_i -th diffusion time step, $z_0^{(i-1)}$ is the output of the $(i-1)$ -th sub-stage; we use $z_0^{(0)}$ to denote the output from the first stage. Then, \mathcal{F} is used to iteratively denoise $z_{T_i}^{(i)}$ from time step T_i to obtain $z_0^{(i)}$. After completing all sub-stages, we obtain $z_0^{(n)}$, which is then decoded to produce the final output $x^{(n)} = \mathcal{D}(z_0^{(n)})$.

We empirically found that generating higher-resolution images requires more sub-stages. Additionally, when refining images using diffusion and denoising, higher resolutions demand larger time steps (Teng et al., 2023). In practice, for flexibility, AP-LDM allows users to customize the number of sub-stages n , and the diffusion time steps T_i for each sub-stage by a pre-specified variable-length progressive scheduler $\eta_2 = \left[\frac{T_1}{T_0}, \frac{T_2}{T_0}, \dots, \frac{T_n}{T_0} \right]$, whose length is n . The elements of η_2 represent the denoising steps of each sub-stage, normalized by T_0 .

4 EXPERIMENTS

4.1 IMPLEMENTATION DETAILS

Experimental settings. We use SDXL (Podell et al., 2023) as the pre-trained LDM and conduct inference using two NVIDIA 4090 GPUs. To ensure consistency when testing inference speed, we use a single NVIDIA 3090 GPU, aligning with other methods. We randomly sample 33k images from the SAM (Kirillov et al., 2023) dataset as the benchmark. Following the released code from DemoFusion (Du et al., 2024), we use the EulerDiscreteScheduler (Karras et al., 2022) setting $T_0 = 50$ and the classifier-free guidance (Ho & Salimans, 2022) scale to 7.5. Pixel space upsampling is performed using bicubic interpolation, and the decay factor β is fixed at 3.

Evaluation metrics. The widely recognized metrics FID (Heusel et al., 2017), IS (Salimans et al., 2016), and CLIP Score (Radford et al., 2021) are used to evaluate model performance. Additionally, since calculating FID and IS requires resizing images to 299×299 , which may not be suitable for evaluating HR images, we are inspired by (Du et al., 2024; Lin et al., 2024) to perform ten 1024×1024 window crops on each image to calculate FID_c and IS_c .

4.2 QUANTITATIVE RESULTS

We compare AP-LDM with the following models: (1) SDXL (Podell et al., 2023); (2) MultiDiffusion (Bar-Tal et al., 2023); (3) ScaleCrafter (He et al., 2023); (4) DemoFusion (Du et al., 2024); (5) Upsample Guidance (UG) (Hwang et al., 2024); (6) AccDiffusion (Lin et al., 2024). For fair comparisons, we disabled the FreeU trick (Si et al., 2024) in all experiments.

Table 1: **Quantitative comparison results.** The best results are marked in **bold**, and the second best results are marked by underline.

Method	2048 × 2048					2048 × 4096					4096 × 2048					4096 × 4096				
	FID	IS	FID _c	IS _c	CLIP	FID	IS	FID _c	IS _c	CLIP	FID	IS	FID _c	IS _c	CLIP	FID	IS	FID _c	IS _c	CLIP
SDXL	99.9	14.2	80.0	16.9	25.0	149.9	9.5	106.3	12.0	24.4	173.1	9.1	108.5	11.5	23.9	191.4	8.3	114.1	12.4	22.9
MultiDiff.	98.8	14.5	67.9	17.1	24.6	125.8	9.6	71.9	15.7	<u>24.6</u>	149.0	9.0	70.5	14.4	<u>24.4</u>	168.4	6.5	76.6	14.4	23.1
ScaleCrafter	98.2	14.2	89.7	13.3	<u>25.4</u>	161.9	10.0	154.3	7.5	23.3	175.1	9.7	167.3	8.0	21.6	164.5	9.4	170.1	7.3	22.3
UG	82.2	17.6	65.8	14.6	<u>25.5</u>	155.7	8.2	165.0	6.6	21.7	185.3	6.8	175.7	6.2	20.5	187.3	7.0	197.6	6.3	21.8
DemoFusion	72.3	21.6	53.5	19.1	25.2	96.3	<u>17.7</u>	<u>62.3</u>	<u>15.0</u>	25.0	<u>99.6</u>	<u>16.4</u>	<u>61.9</u>	<u>14.7</u>	<u>24.4</u>	<u>101.4</u>	<u>20.7</u>	<u>63.5</u>	<u>13.5</u>	24.7
AccDiff.	71.6	<u>21.0</u>	<u>52.7</u>	17.0	25.1	<u>95.5</u>	16.4	62.9	11.1	24.5	<u>102.2</u>	15.2	63.4	11.5	24.2	103.2	20.1	65.9	13.3	<u>24.6</u>
AP-LDM	66.0	<u>21.0</u>	47.4	<u>17.5</u>	25.1	89.0	20.3	56.0	19.0	25.0	93.2	19.5	56.9	16.5	24.9	90.6	21.1	59.0	14.8	<u>24.6</u>

We report the performance of all methods on four different resolutions (Height × Width): 4096×4096 , 4096×2048 , 2048×4096 , and 2048×2048 . Considering that the generation time for HR images far exceeds that for low-resolution images, we used 2k prompts at the resolution of 2048×2048 , and 1k prompts for resolutions greater 2048×2048 . For all resolutions, we set $\gamma = 0.004$ and $\eta_1 = 0.06$ for AP-LDM. Given that the 4096×4096 resolution is significantly larger than other resolutions, we set $\eta_2 = [0.1, 0.2]$ (i.e., $T_0 = 50$, $T_1 = 5$, $T_2 = 10$) for 4096×4096 , and $\eta_2 = [0.2]$ (i.e., $T_0 = 50$ and $T_1 = 10$) for other resolutions. When generating images with an aspect ratio of r' , we reshape the initially sampled Gaussian noise ϵ in the first stage to match r' . This process keeps the number of tokens in ϵ unchanged, preventing drastic fluctuations in the entropy of the attention maps in the transformer (Jin et al., 2024) leading to higher-quality images.

Table 1 manifests that AP-LDM significantly outperforms previous SOTA models, AccDiffusion and DemoFusion. This indicates that AP-LDM generates images with higher quality. Notably, Table 2 indicates that AP-LDM demonstrates remarkable advantage in inference speed compared to the SOTA models. On a consumer-grade 3090 GPU, AP-LDM requires only about one-fifth of the inference time needed by SOTA models such as DemoFusion and AccDiffusion.

Table 2: **Model inference time.** The best results are marked in **bold**. Unit of Time: minute.

Resolutions	SDXL	MultiDiff.	ScaleCrafter	UG	DemoFusion	AccDiff.	AP-LDM
2048×2048	1.0	3.0	1.0	1.8	3.0	3.0	0.6
2048×4096	3.0	6.0	6.0	4.0	11.0	12.7	2.0
4096×4096	8.0	15.0	19.0	11.1	25.0	26.0	5.7

4.3 QUALITATIVE RESULTS

In Fig. 5, AP-LDM is qualitatively compared with AccDiffusion, DemoFusion, and MultiDiffusion. MultiDiffusion fails to maintain global semantic consistency. As indicated by the red boxes, DemoFusion and AccDiffusion tend to result in chaotic content repetition and severe artifacts, which we speculate are caused by upsampling in the latent space (as analyzed in §3.3). In contrast, AP-LDM not only preserves excellent global structural consistency but also synthesizes images with more details. More qualitative comparison results can be found in Appendix A.3.

4.4 USER STUDY

We invite 16 volunteers to participate in a double-blind experiment to further evaluate the performance of the models. Each volunteer is required to answer 35 questions. In each question, three images generated by AccDiffusion, DemoFusion, and SwiftFusion are presented. The volunteer needs to rate each image from 1 to 10 in terms of structural consistency, color abundance, and detail richness. We calculate the average of their scores. Moreover, to eliminate bias in each volunteer’s ratings for each metric in each question, we subtract the minimum value among the three scores given by each volunteer for each metric in each question. The rectified score is denoted as score*. Table 3 shows that AP-LDM surpasses previous SOTA models across all metrics.

Table 3: **Results of the user study.**

Method	Structural Consistency		Color Abundance		Detail Richness	
	score \uparrow	score* \uparrow	score \uparrow	score* \uparrow	score \uparrow	score* \uparrow
AccDiffusion	6.28	0.88	6.78	0.60	6.18	0.53
DemoFusion	5.99	0.59	6.69	0.51	6.18	0.53
AP-LDM	7.42	2.02	7.64	1.45	7.41	1.76

5 ABLATION STUDY

5.1 ATTENTIVE GUIDANCE

In this section, we first conduct ablation experiments on attentive guidance, followed by ablation experiments on the hyper-parameters of attentive guidance.

Ablation on attentive guidance. We keep η_2 unchanged and analyze the effect of attentive guidance through qualitative and quantitative experiments. Table. 4 shows that attentive guidance leads to improvements across various metrics, indicating that using attentive guidance to enhance the consistency of latent encoding results in higher-quality images. The qualitative experiments in Fig. 6 demonstrate that using attentive guidance eliminates image blurriness and enriches the image details. Please refer to Appendix A.2.1 for additional qualitative ablation results.

Table 4: **Ablation on attentive guidance (AG).** The best results are marked in **bold**.

Method	2048×2048					2048×4096					4096×2048					4096×4096				
	FID	IS	FID _c	IS _c	CLIP	FID	IS	FID _c	IS _c	CLIP	FID	IS	FID _c	IS _c	CLIP	FID	IS	FID _c	IS _c	CLIP
w/o AG	66.8	21.6	47.5	17.4	25.3	91.6	20.3	58.0	14.5	25.0	95.3	19.9	58.4	14.5	24.9	92.0	21.6	59.8	13.6	24.5
w/ AG	66.0	21.0	47.4	17.5	25.1	89.0	20.3	56.0	19.0	25.0	93.2	19.5	56.9	16.5	24.9	90.6	21.1	59.0	14.8	24.6

Ablation on guidance scale γ . We fix $\eta_1 = 0.06, \eta_2 = [0.2]$ and then explore the effect of the guidance scale γ through both quantitative and qualitative experiments. For the quantitative experiments, we find that $\gamma = 0.004$ performs better. Interestingly, when a larger guidance scale is used, the visual quality of the images can be further enhanced. As shown in Fig. 7, using a larger guidance scale results in richer image details. This allows users to generate images according to their preferences for detail richness and color contrast by adjusting the guidance scale. The setup and results of the quantitative experiments are detailed in Appendix A.2.1.

Ablation on delay rate η_1 . We fix $\gamma = 0.004, \eta_2 = [0.2]$ and then investigate the impact of the delay rate η_1 through both quantitative and qualitative experiments. The quantitative analysis results



Figure 5: **Qualitative comparison with other baselines.** The prompts used to generate the images are presented on the right. MultiDiffusion fails to maintain global semantic consistency. DemoFusion and AccDiffusion exhibit severe artifacts and content repetition. The red boxes indicate some synthesis errors.



Figure 6: **Generating with and without attentive guidance.** Resolution: 2048×2048 . Zoom-in for a better view.

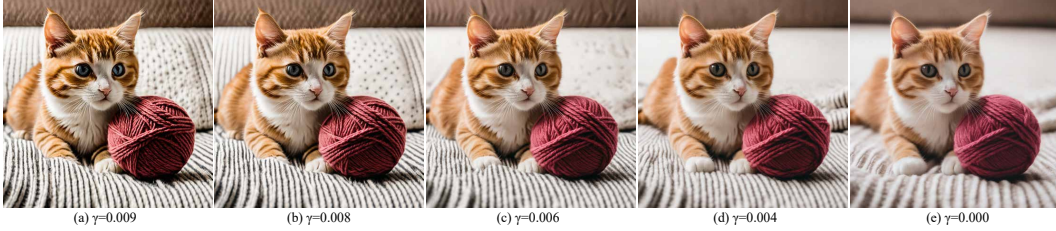


Figure 7: **Generating images using different guidance scale.** Resolution: 2048×2048 .

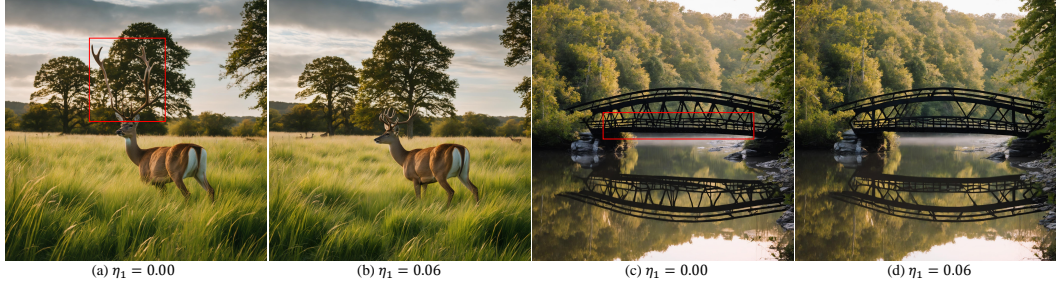


Figure 8: **Ablation on delay rate.** Errors indicated by red boxes can be eliminated by delaying attentive guidance. Resolution: 2048×2048 .

indicate that better generation results can be achieved when $\eta_1 = 0.06$, indicating that appropriately delaying the effect of attentive guidance contributes to further improving the quality of the images. We conjecture that this is because, at the very beginning of the denoising process, the structural information in the latent encoding has not yet emerged, and thus attentive guidance cannot effectively enhance structural consistency. As shown in Fig. 8, delaying the effect of attentive guidance eliminates some generation errors, further improving image quality. The setup and results of the quantitative experiments are detailed in Appendix A.2.1.

Ablation on the time steps of attentive guidance. To explain why attentive guidance needs to be applied during the early to middle steps of denoising, we apply attentive guidance during different denoising steps of the first stage: (a) 47 to 33, (b) 32 to 17, and (c) 16 to 1. Fig. 9 shows that when attentive guidance is applied during the early to middle steps of denoising, the image becomes clearer and more detailed; however, when attentive guidance is applied during the later steps of denoising, it has negligible effect on the generated image. We speculate that this is because diffusion models tend to synthesize structural information first (Teng et al., 2023), and once the structural information is generated, attentive guidance may have a limited impact on structural consistency.

5.2 PROGRESSIVE HIGH-RESOLUTION DENOISING

In this section, we conduct ablation experiments on the progressive scheduler η_2 in the second stage of AP-LDM. Specifically, we fixed $\gamma = 0, \eta_1 = 0$ and then explore the effect of the progressive scheduler η_2 through both quantitative and qualitative experiments. Quantitative experimental results indicate that an excessively large progressive scheduler value may result in a decline in image quality. This can also be observed in Fig. 10. It is evident that a too large progressive scheduler value may lead to structural misalignment and repetition issues observed in pre-trained SDXL. When the



Figure 9: **Applying attentive guidance at different denoising steps.** Resolution: 2048×2048 .

progressive scheduler value is sufficiently small, changing it yields similar visual effects. Therefore, we can choose a smaller progressive scheduler value (*e.g.*, 0.2) to accelerate inference. The setup and quantitative results are detailed in Appendix A.2.2.



Figure 10: **Generated 2048×2048 images using different η_2 .** (a): When the value of progressive scheduler is too large, the structural repetition issue may reappear. (b) to (e): The visual effects are similar. Therefore, we can use a smaller progressive scheduler value to accelerate inference.

6 LIMITATIONS AND FUTURE WORK

AP-LDM exhibits limitations in the following aspects: (i) Effectively controlling text in images is challenging, as demonstrated by examples in Fig. 11. This may be due to the inherent limitations of SDXL in generating textual symbols. Text, due to its more regular structure compared to other image content, is difficult to restore by directly enhancing the structural consistency of the latent representation. We speculate that the most reliable approach would be to fine-tune the model specifically on images containing text. (ii) When generating ultra-high resolution images, such as 12800×12800 , the second stage of AP-LDM inevitably needs to be decomposed into more sub-stages, which increases the model’s inference time.

Developing a low-cost and effective fine-tuning method to correct text generation errors may be a promising direction. Moreover, adapting attentive guidance to other tasks, such as video generation can be an interesting issue.



Figure 11: **Limitations of AP-LDM.** The generation results of SDXL at its training resolution and those of AP-LDM at higher resolutions are provided.

7 CONCLUSION

In this paper, we propose an effective, efficient, and training-free pipeline named AP-LDM, capable of generating HR images with higher quality while accelerating the generation process. AP-LDM

divides the denoising process of an LDM into two stages: (i) attentive training-resolution denoising, and (ii) progressive high-resolution denoising. The first stage aims to generate a latent representation through the proposed attentive guidance, which enhances the structural consistency by leveraging a novel parameter-free self-attention mechanism. The second stage iteratively performs upsampling in the pixel stage, thus eliminating the artifacts caused by latent space upsampling. Extensive experiments show that our proposed AP-LDM significantly outperforms SOTA models while achieving $5\times$ speedup in HR image generation.

REFERENCES

- Omer Bar-Tal, Lior Yariv, Yaron Lipman, and Tali Dekel. Multidiffusion: Fusing diffusion paths for controlled image generation. 2023.
- Jia Deng, Wei Dong, Richard Socher, Li-Jia Li, Kai Li, and Li Fei-Fei. Imagenet: A large-scale hierarchical image database. In *2009 IEEE conference on computer vision and pattern recognition*, pp. 248–255. Ieee, 2009.
- Alexey Dosovitskiy, Lucas Beyer, Alexander Kolesnikov, Dirk Weissenborn, Xiaohua Zhai, Thomas Unterthiner, Mostafa Dehghani, Matthias Minderer, Georg Heigold, Sylvain Gelly, et al. An image is worth 16x16 words: Transformers for image recognition at scale. *arXiv preprint arXiv:2010.11929*, 2020.
- Ruoyi Du, Dongliang Chang, Timothy Hospedales, Yi-Zhe Song, and Zhanyu Ma. Demofusion: Democratising high-resolution image generation with no \$\$\$\$. In *Proceedings of the IEEE/CVF Conference on Computer Vision and Pattern Recognition*, pp. 6159–6168, 2024.
- Patrick Esser, Sumith Kulal, Andreas Blattmann, Rahim Entezari, Jonas Müller, Harry Saini, Yam Levi, Dominik Lorenz, Axel Sauer, Frederic Boesel, et al. Scaling rectified flow transformers for high-resolution image synthesis. In *Forty-first International Conference on Machine Learning*, 2024.
- Zhida Feng, Zhenyu Zhang, Xintong Yu, Yewei Fang, Lanxin Li, Xuyi Chen, Yuxiang Lu, Jiayang Liu, Weichong Yin, Shikun Feng, et al. Ernie-vilg 2.0: Improving text-to-image diffusion model with knowledge-enhanced mixture-of-denoising-experts. In *Proceedings of the IEEE/CVF Conference on Computer Vision and Pattern Recognition*, pp. 10135–10145, 2023.
- Lanqing Guo, Yingqing He, Haoxin Chen, Menghan Xia, Xiaodong Cun, Yufei Wang, Siyu Huang, Yong Zhang, Xintao Wang, Qifeng Chen, et al. Make a cheap scaling: A self-cascade diffusion model for higher-resolution adaptation. *arXiv preprint arXiv:2402.10491*, 2024.
- Moayed Haji-Ali, Guha Balakrishnan, and Vicente Ordonez. Elasticdiffusion: Training-free arbitrary size image generation. *arXiv preprint arXiv:2311.18822*, 2023.
- Kai Han, An Xiao, Enhua Wu, Jianyuan Guo, Chunjing Xu, and Yunhe Wang. Transformer in transformer. *Advances in neural information processing systems*, 34:15908–15919, 2021.
- Yingqing He, Shaoshu Yang, Haoxin Chen, Xiaodong Cun, Menghan Xia, Yong Zhang, Xintao Wang, Ran He, Qifeng Chen, and Ying Shan. Scalecrafter: Tuning-free higher-resolution visual generation with diffusion models. In *The Twelfth International Conference on Learning Representations*, 2023.
- Martin Heusel, Hubert Ramsauer, Thomas Unterthiner, Bernhard Nessler, and Sepp Hochreiter. Gans trained by a two time-scale update rule converge to a local nash equilibrium. *Advances in neural information processing systems*, 30, 2017.
- Jonathan Ho and Tim Salimans. Classifier-free diffusion guidance. *arXiv preprint arXiv:2207.12598*, 2022.
- Jonathan Ho, Ajay Jain, and Pieter Abbeel. Denoising diffusion probabilistic models. *Advances in neural information processing systems*, 33:6840–6851, 2020.

-
- Jonathan Ho, Chitwan Saharia, William Chan, David J Fleet, Mohammad Norouzi, and Tim Salimans. Cascaded diffusion models for high fidelity image generation. *Journal of Machine Learning Research*, 23(47):1–33, 2022.
- Emiel Hooeboom, Jonathan Heek, and Tim Salimans. simple diffusion: End-to-end diffusion for high resolution images. In *International Conference on Machine Learning*, pp. 13213–13232. PMLR, 2023.
- Juno Hwang, Yong-Hyun Park, and Junghyo Jo. Upsample guidance: Scale up diffusion models without training. *arXiv preprint arXiv:2404.01709*, 2024.
- Zhiyu Jin, Xuli Shen, Bin Li, and Xiangyang Xue. Training-free diffusion model adaptation for variable-sized text-to-image synthesis. *Advances in Neural Information Processing Systems*, 36, 2024.
- Tero Karras, Miika Aittala, Timo Aila, and Samuli Laine. Elucidating the design space of diffusion-based generative models. *Advances in neural information processing systems*, 35:26565–26577, 2022.
- Alexander Kirillov, Eric Mintun, Nikhila Ravi, Hanzi Mao, Chloe Rolland, Laura Gustafson, Tete Xiao, Spencer Whitehead, Alexander C Berg, Wan-Yen Lo, et al. Segment anything. In *Proceedings of the IEEE/CVF International Conference on Computer Vision*, pp. 4015–4026, 2023.
- Yuseung Lee, Kunho Kim, Hyunjin Kim, and Minhyuk Sung. Syncdiffusion: Coherent montage via synchronized joint diffusions. *Advances in Neural Information Processing Systems*, 36:50648–50660, 2023.
- Jingyun Liang, Jiezhong Cao, Guolei Sun, Kai Zhang, Luc Van Gool, and Radu Timofte. Swinir: Image restoration using swin transformer. In *Proceedings of the IEEE/CVF international conference on computer vision*, pp. 1833–1844, 2021.
- Zhihang Lin, Mingbao Lin, Meng Zhao, and Rongrong Ji. Accdiffusion: An accurate method for higher-resolution image generation. *arXiv preprint arXiv:2407.10738*, 2024.
- Ze Liu, Yutong Lin, Yue Cao, Han Hu, Yixuan Wei, Zheng Zhang, Stephen Lin, and Baining Guo. Swin transformer: Hierarchical vision transformer using shifted windows. In *Proceedings of the IEEE/CVF international conference on computer vision*, pp. 10012–10022, 2021.
- Xiaotong Luo, Zekun Ai, Qiuyuan Liang, Ding Liu, Yuan Xie, Yanyun Qu, and Yun Fu. Adaformer: Efficient transformer with adaptive token sparsification for image super-resolution. In *Proceedings of the AAAI Conference on Artificial Intelligence*, volume 38, pp. 4009–4016, 2024.
- Chong Mou, Xintao Wang, Liangbin Xie, Yanze Wu, Jian Zhang, Zhongang Qi, and Ying Shan. T2i-adapter: Learning adapters to dig out more controllable ability for text-to-image diffusion models. In *Proceedings of the AAAI Conference on Artificial Intelligence*, volume 38, pp. 4296–4304, 2024.
- Alexander Quinn Nichol and Prafulla Dhariwal. Improved denoising diffusion probabilistic models. In *International conference on machine learning*, pp. 8162–8171. PMLR, 2021.
- Dustin Podell, Zion English, Kyle Lacey, Andreas Blattmann, Tim Dockhorn, Jonas Müller, Joe Penna, and Robin Rombach. Sdxl: Improving latent diffusion models for high-resolution image synthesis. *arXiv preprint arXiv:2307.01952*, 2023.
- Alec Radford, Jong Wook Kim, Chris Hallacy, Aditya Ramesh, Gabriel Goh, Sandhini Agarwal, Girish Sastry, Amanda Askell, Pamela Mishkin, Jack Clark, et al. Learning transferable visual models from natural language supervision. In *International conference on machine learning*, pp. 8748–8763. PMLR, 2021.
- Tim Salimans, Ian Goodfellow, Wojciech Zaremba, Vicki Cheung, Alec Radford, and Xi Chen. Improved techniques for training gans. *Advances in neural information processing systems*, 29, 2016.

-
- Chenyang Si, Ziqi Huang, Yuming Jiang, and Ziwei Liu. Freeu: Free lunch in diffusion u-net. In *Proceedings of the IEEE/CVF Conference on Computer Vision and Pattern Recognition*, pp. 4733–4743, 2024.
- Jiayan Teng, Wendi Zheng, Ming Ding, Wenyi Hong, Jianqiao Wangni, Zhuoyi Yang, and Jie Tang. Relay diffusion: Unifying diffusion process across resolutions for image synthesis. *arXiv preprint arXiv:2309.03350*, 2023.
- Ashish Vaswani, Noam Shazeer, Niki Parmar, Jakob Uszkoreit, Llion Jones, Aidan N Gomez, Łukasz Kaiser, and Illia Polosukhin. Attention is all you need. *Advances in neural information processing systems*, 30, 2017.
- Jianyi Wang, Zongsheng Yue, Shangchen Zhou, Kelvin CK Chan, and Chen Change Loy. Exploiting diffusion prior for real-world image super-resolution. *arXiv preprint arXiv:2305.07015*, 2023.
- Yang Wang and Tao Zhang. Osffnet: Omni-stage feature fusion network for lightweight image super-resolution. In *Proceedings of the AAAI Conference on Artificial Intelligence*, volume 38, pp. 5660–5668, 2024.
- Jiwen Yu, Yinhuai Wang, Chen Zhao, Bernard Ghanem, and Jian Zhang. Freedom: Training-free energy-guided conditional diffusion model. In *Proceedings of the IEEE/CVF International Conference on Computer Vision*, pp. 23174–23184, 2023.
- Kai Zhang, Jingyun Liang, Luc Van Gool, and Radu Timofte. Designing a practical degradation model for deep blind image super-resolution. In *Proceedings of the IEEE/CVF International Conference on Computer Vision*, pp. 4791–4800, 2021.
- Lvmin Zhang, Anyi Rao, and Maneesh Agrawala. Adding conditional control to text-to-image diffusion models. In *Proceedings of the IEEE/CVF International Conference on Computer Vision*, pp. 3836–3847, 2023.
- Qingping Zheng, Yuanfan Guo, Jiankang Deng, Jianhua Han, Ying Li, Songcen Xu, and Hang Xu. Any-size-diffusion: Toward efficient text-driven synthesis for any-size hd images. In *Proceedings of the AAAI Conference on Artificial Intelligence*, volume 38, pp. 7571–7578, 2024.
- Yupeng Zhou, Daquan Zhou, Ming-Ming Cheng, Jiashi Feng, and Qibin Hou. Storydiffusion: Consistent self-attention for long-range image and video generation. *arXiv preprint arXiv:2405.01434*, 2024.

Algorithm 1 AP-LDM Inference Pipeline

Require: The number of inference time steps of the first stage T_0 ; progressive scheduler η_2 ; attentive guidance scale γ ; attentive guidance delay rate η_1 ; the decay factor β ; target image size tuple (H', W') ; the denoising model \mathcal{F} ; denoising model’s training resolution tuple (H, W) ; VAE encoder \mathcal{E} ; VAE decoder \mathcal{D} ; noise scheduler’s hyper-parameter list $\bar{\alpha}_{1:T_0}$.

```
1: Initialization:
2:  $\mathbf{z}_{T_0}^{(0)} = \epsilon \sim \mathcal{N}(0, \mathbf{I})$  ▷ Sampling from Standard Gaussian Distribution
3:  $n_{\text{stages}} = \text{length}(\eta_2) + 1$  ▷ Get the total number of denoising stages
4:  $r' = \frac{H'}{W'}$  ▷ Keep the aspect ratio and number of pixels unchanged
5:  $H^{(0)} = \text{ceil}(\sqrt{H \times W \times r'})$ 
6:  $W^{(0)} = \text{ceil}(\sqrt{\frac{H \times W}{r'}})$ 
7:  $H^{(n)} = H'$ 
8:  $W^{(n)} = W'$ 
9:  $\text{area}_{\text{list}} = \text{linspace}(H^{(0)} \times W^{(0)}, H^{(n)} \times W^{(n)}, n_{\text{stages}})$  ▷ Upsampling according to the number of pixels
10:  $H_{\text{list}} = [\text{ceil}(\sqrt{i \times r'}) \text{ for } i \text{ in } \text{area}_{\text{list}}]$  ▷ Get the height and width of each stage
11:  $W_{\text{list}} = [\text{ceil}(\sqrt{i/r'}) \text{ for } i \text{ in } \text{area}_{\text{list}}]$ 
12:  $k_{\text{denoising}} = [T_0]$  ▷ Get the number of denoising steps for each stage
13:  $k_{\text{denoising}}.\text{extend}([i \times T_0 \text{ for } i \text{ in } \eta_2])$ 
14:  $k = T_0 \times \eta_1$  ▷ Obtain the number of delay steps
15:  $\gamma_{\text{list}} = [\gamma(\frac{\cos(\frac{T-k-i}{T-k}\pi)+1}{2})^\beta \text{ for } i = 1, \dots, T-k]$  ▷ Obtain the guidance scale for each step
16: Denoising:
17: for  $s = 0, \dots, n_{\text{stages}} - 1$  do:
18:    $n_{\text{steps}} \leftarrow k_{\text{denoising}}[s]$ 
19:   if  $s \geq 1$  then:
20:      $\mathbf{x}^{(s)} \leftarrow \text{upsample}(\mathbf{x}^{(s-1)}, H_{\text{list}}[s], W_{\text{list}}[s])$  ▷ Upsampling in pixel space
21:      $\mathbf{z}_0^{(s)} \leftarrow \mathcal{E}(\mathbf{x}^{(s)})$ 
22:      $\mathbf{z}_{n_{\text{steps}}}^{(s)} \sim \mathcal{N}(\sqrt{\bar{\alpha}[n_{\text{steps}}]}\mathbf{z}_0^{(s)}, (1 - \bar{\alpha}[n_{\text{steps}}])\mathbf{I})$ 
23:   end if
24:   for  $t = n_{\text{steps}} - 1, \dots, 0$  do:
25:      $\mathbf{z}_t^{(s)} \leftarrow \mathcal{F}(\mathbf{z}_{t+1}^{(s)}, t + 1)$  ▷ Denoising
26:     if  $s == 0$  and  $t \leq T - 1 - k$  then:
27:        $\mathbf{z}_t^{(s)} \leftarrow \gamma_{\text{list}}[t]\text{PFSA}(\mathbf{z}_t^{(s)}) + (1 - \gamma_{\text{list}}[t])\mathbf{z}_t^{(s)}$  ▷ Attentive Guidance
28:     end if
29:   end for
30:    $\mathbf{x}^{(s)} \leftarrow \mathcal{D}(\mathbf{z}_0^{(s)})$  ▷ Obtain the pixel space image
31: end for
```

A APPENDIX

A.1 AP-LDM ALGORITHM

The implementation details of AP-LDM can be found in Algorithm 1, and further information is available in our code repository.

A.2 FURTHER RESULTS OF ABLATION STUDIES

A.2.1 ATTENTIVE GUIDANCE

Quantitative analysis of guidance scale. We sampled 1k prompts, fixed $\eta_1 = 0.06$, $\eta_2 = [0.2]$ and performed ablation studies for guidance scale γ . The quantitative results are shown in Table 5. Considering all metrics, we find that $\gamma = 0.004$ achieved better quantitative results.

Quantitative analysis of delay rate. We sampled 1k prompts, fixed $\gamma = 0.004$, $\eta_2 = [0.2]$ and performed ablation studies for delay rate η_1 . Table 6 presents the experimental results, indicating that better results can be achieved when $\eta_1 = 0.06$. This means that appropriately delaying the effect of attentive guidance can further enhance the quality of the generated images.

Further qualitative analysis of attentive guidance. Fig. 12 provides additional qualitative ablation results on attentive guidance. Individual preferences for contrast, color vividness, and detail

Method	1024 × 1024					1600 × 1600					2048 × 2048				
	FID ↓	IS ↑	FID _c ↓	IS _c ↑	CLIP ↑	FID ↓	IS ↑	FID _c ↓	IS _c ↑	CLIP ↑	FID ↓	IS ↑	FID _c ↓	IS _c ↑	CLIP ↑
$\gamma = 0.000$	90.85	58.18	21.21	17.69	25.09	90.91	54.74	21.45	15.41	24.93	91.78	59.08	<u>21.57</u>	<u>17.36</u>	24.86
$\gamma = 0.001$	90.50	58.04	21.34	16.76	25.08	91.17	54.31	21.19	<u>15.47</u>	24.93	91.40	58.75	21.87	15.85	24.86
$\gamma = 0.002$	89.82	57.54	<u>21.28</u>	<u>17.04</u>	25.08	90.39	53.71	21.26	15.00	24.97	90.81	<u>58.34</u>	21.45	17.16	24.90
$\gamma = 0.003$	90.10	<u>57.08</u>	20.80	16.61	25.08	90.56	<u>53.95</u>	<u>21.35</u>	15.46	24.98	90.87	<u>58.40</u>	21.47	17.60	24.92
$\gamma = 0.004$	89.40	56.64	20.96	16.63	25.09	89.91	54.23	20.91	15.54	25.01	90.11	58.11	21.18	16.78	24.94s
$\gamma = 0.005$	90.17	57.50	20.89	16.34	25.12	<u>90.24</u>	55.19	20.67	15.21	25.02	90.46	58.91	20.79	16.87	24.97
$\gamma = 0.006$	<u>89.79</u>	58.18	20.33	15.93	25.16	90.36	56.71	20.33	14.59	25.06	<u>90.32</u>	59.86	20.37	16.12	25.00
$\gamma = 0.007$	90.42	60.29	20.07	16.20	25.21	90.91	59.35	20.36	14.16	25.12	90.86	61.81	20.14	15.70	25.06
$\gamma = 0.008$	91.64	63.63	19.66	14.25	25.25	91.98	63.93	19.13	13.71	<u>25.13</u>	92.16	64.82	19.59	14.24	<u>25.08</u>
$\gamma = 0.009$	94.29	67.87	19.15	13.00	<u>25.25</u>	94.38	70.21	19.45	12.12	25.16	94.39	68.84	19.22	13.63	25.12

Table 5: **Quantitative ablation experiments on the guidance scale γ .** The best results are marked in **bold**, and the second best results are marked by underline.

Method	1024 × 1024					1600 × 1600					2048 × 2048				
	FID ↓	IS ↑	FID _c ↓	IS _c ↑	CLIP ↑	FID ↓	IS ↑	FID _c ↓	IS _c ↑	CLIP ↑	FID ↓	IS ↑	FID _c ↓	IS _c ↑	CLIP ↑
$\eta_1 = 0.00$	89.98	58.29	20.74	16.48	25.06	90.89	55.54	21.00	14.42	24.98	90.75	59.41	20.54	16.99	24.91
$\eta_1 = 0.02$	89.96	57.67	20.99	16.87	25.05	90.76	54.77	21.08	15.35	24.95	91.78	59.08	21.57	18.16	24.86
$\eta_1 = 0.04$	89.47	57.28	20.98	16.63	25.07	90.22	54.14	20.86	15.43	24.98	90.52	58.47	20.76	17.02	24.91
$\eta_1 = 0.06$	<u>89.44</u>	56.64	20.92	16.58	25.11	<u>89.91</u>	54.23	20.91	15.54	25.01	90.11	58.11	21.18	16.78	24.94
$\eta_1 = 0.08$	89.95	56.97	21.05	16.76	25.09	89.87	54.10	21.22	<u>15.65</u>	24.98	90.74	58.45	20.99	17.06	24.92
$\eta_1 = 0.10$	89.29	<u>56.88</u>	21.11	<u>16.84</u>	25.09	89.97	53.99	21.04	15.37	<u>24.99</u>	90.41	58.45	20.99	17.12	<u>24.92</u>
$\eta_1 = 0.12$	89.84	57.32	21.05	16.58	25.08	90.00	53.85	21.24	15.81	24.93	<u>90.24</u>	58.45	<u>21.24</u>	<u>17.36</u>	24.90
$\eta_1 = 0.14$	89.85	57.12	20.91	16.40	<u>25.09</u>	90.06	<u>53.83</u>	<u>21.33</u>	15.62	24.99	90.69	<u>58.25</u>	21.17	16.74	24.91
$\eta_1 = 0.16$	90.06	57.28	<u>21.10</u>	16.53	25.09	90.91	54.74	21.45	15.41	24.93	90.76	58.37	20.97	16.87	24.91
$\eta_1 = 0.18$	90.16	57.29	20.88	15.10	25.08	90.26	53.79	21.06	15.07	24.97	90.78	58.33	21.05	17.21	24.90

Table 6: **Quantitative ablation experiments on the delay rate η_1 .** The best results are marked in **bold**, and the second best results are marked by underline.

richness may vary. attentive guidance allows users to adjust parameters such as the guidance scale to synthesize images according to their preferences.

A.2.2 PROGRESSIVE HIGH-RESOLUTION DENOISING

This section presents the results of quantitative ablation analysis on the progressive scheduler η_2 in the second stage of AP-LDM. We fixed $\gamma = 0$, $\eta_1 = 0$, sampled 500 prompts, and generated 1k images to investigate the optimal value of the progressive scheduler. Table 7 presents the quantitative results, indicating that using an excessively large progressive scheduler may lead to a decline in image quality.

Method	1600 × 1600					2048 × 2048				
	FID ↓	IS ↑	FID _c ↓	IS _c ↑	CLIP ↑	FID ↓	IS ↑	FID _c ↓	IS _c ↑	CLIP ↑
SDXL	101.56	25.78	73.67	21.23	26.87	112.64	18.44	79.03	20.61	26.55
$\eta_2 = [0.9]$	94.59	27.04	67.60	23.01	26.97	97.14	24.48	64.34	22.14	26.59
$\eta_2 = [0.8]$	93.13	28.80	65.67	24.83	26.99	93.93	26.75	60.84	23.27	26.77
$\eta_2 = [0.7]$	92.05	29.44	65.35	24.97	27.07	92.50	28.17	57.34	24.05	26.93
$\eta_2 = [0.6]$	92.94	30.79	64.57	24.29	27.11	91.86	30.45	55.38	24.96	26.98
$\eta_2 = [0.5]$	<u>92.73</u>	30.65	63.43	24.26	27.13	<u>91.80</u>	<u>31.18</u>	54.32	24.48	27.02
$\eta_2 = [0.4]$	93.04	<u>30.96</u>	63.33	24.77	27.14	91.71	32.47	53.72	25.16	27.03
$\eta_2 = [0.3]$	92.93	30.91	63.09	24.84	27.15	92.39	30.72	<u>53.32</u>	26.63	27.07
$\eta_2 = [0.2]$	93.09	31.17	<u>63.23</u>	25.71	27.17	92.71	30.45	53.19	26.19	27.12
$\eta_2 = [0.1]$	93.44	30.69	63.75	<u>25.18</u>	27.22	92.94	30.69	53.77	24.71	27.18

Table 7: **Quantitative ablation study of the progressive scheduler.** The best results are marked in **bold**, and the second best results are marked by underline.

A.3 SUPPLEMENTARY QUALITATIVE ANALYSIS

Fig. 13 presents additional qualitative comparison results. MultiDiffusion continues to struggle with maintaining global consistency; as indicated by the red boxes, DemoFusion tends to produce repetitive content, a problem somewhat alleviated in AccDiffusion but not fully resolved. As highlighted by the black boxes, another issue with AccDiffusion is the presence of noticeable streak artifacts in the images.

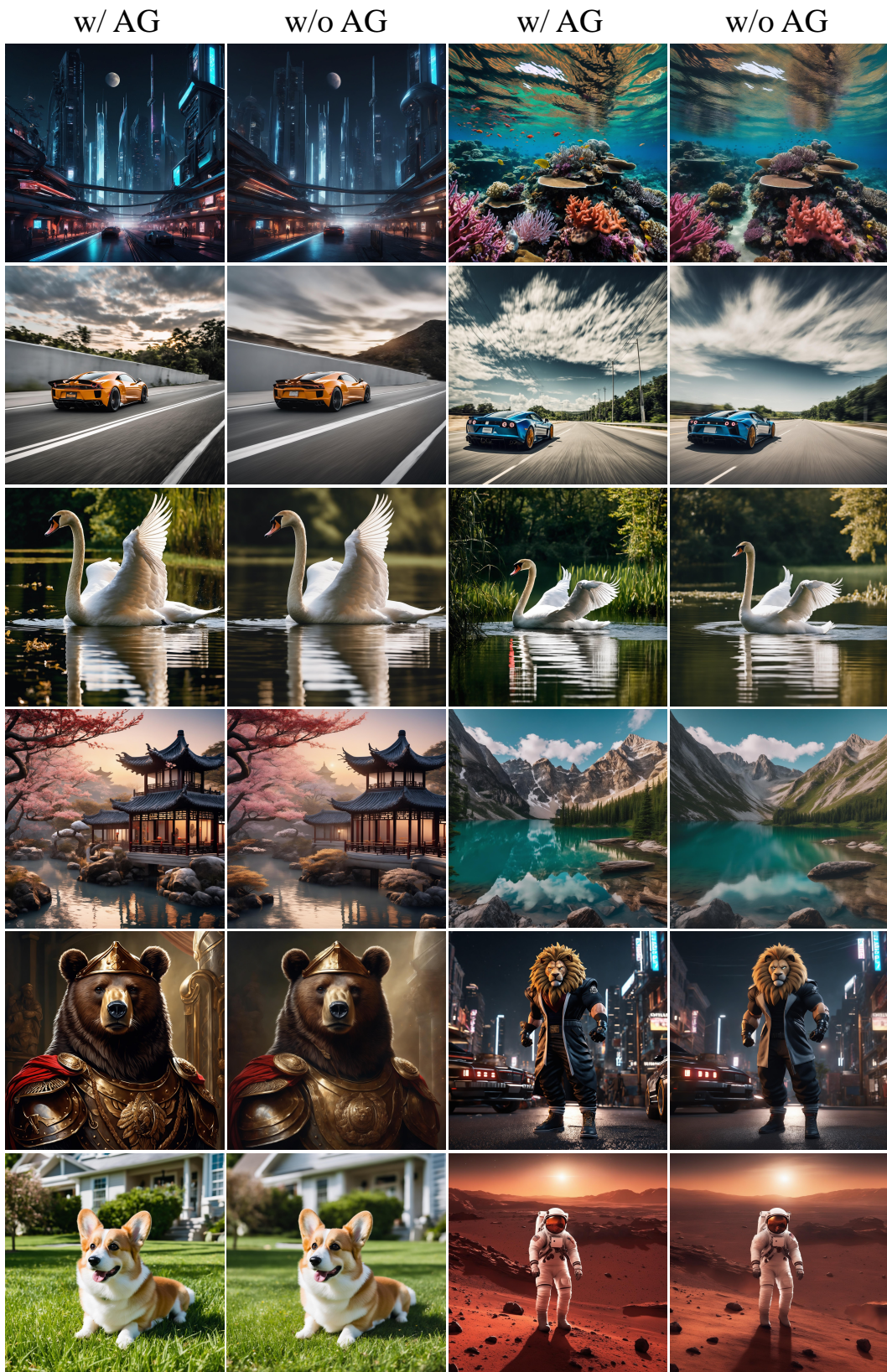


Figure 12: **Further qualitative analysis of attentive guidance (AG).** Using attentive guidance significantly enhances image quality. The details were enriched, for example: the clouds in the sky, ripples on the water, reflections on the lake, and even the expressions in a person’s eyes. Best viewed **ZOOMED-IN**.

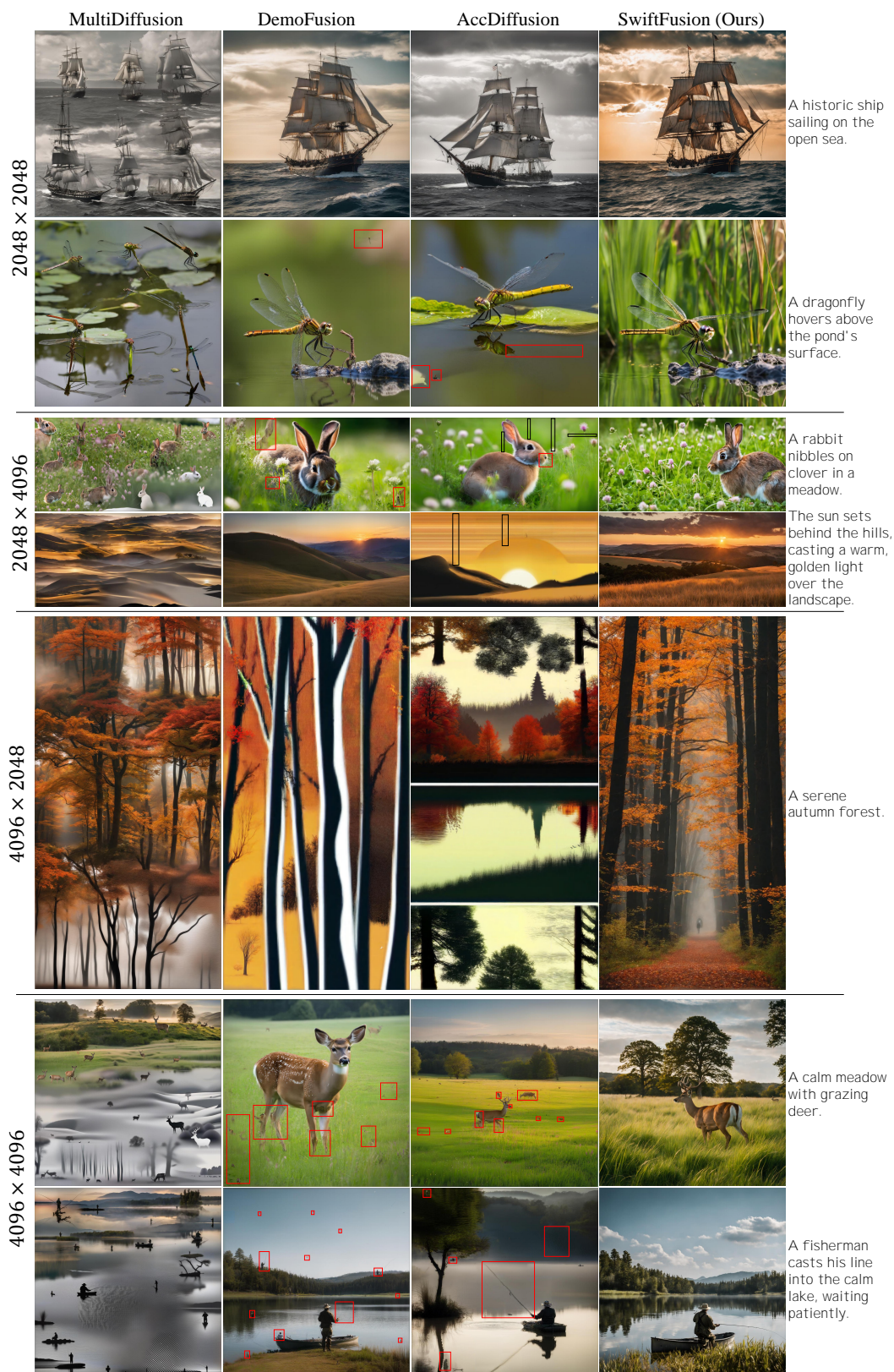


Figure 13: Qualitative comparison with other baselines.